Supplementary Materials

ZIF-supported AuCu Nanoalloy for Ammonia Electrosynthesis from Nitrogen and Thin Air

Xian-Wei Lv,[a] Lu Wang,[b] Guichang Wang,[a] Ran Hao,[a] Jin-Tao Ren,[a] Xiaolu Liu,[a] Paul N. Duchesne,[b] Yuping Liu,*[a] Wei Li,[a] Zhong-Yong Yuan,[a] Geoffrey A. Ozin,*[b]

[a] *Key Laboratory of Advanced Energy Materials Chemistry (Ministry of Education), College of Chemistry, School of Materials Science and Engineering, Nankai University, Tianjin 300071, China. E-mail: liuypnk@nankai.edu.cn*

[b] *Materials Chemistry and Nanochemistry Research Group, Solar Fuels Cluster, Department of Chemistry, University of Toronto, 80 St. George Street, Toronto, Ontario M5S3H6, Canada. E-mail: gozin@chem.utoronto.ca*

Experimental Section

Chemicals and materials

$NaBH_4$, $CuCl_2 \cdot 2H_2O$, $Zn(NO_3)_2 \cdot 6(H_2O)$ and 2-Methylimidazole were purchased from Tianjin Guangfu Chemical Co. Other chemicals were purchased from various companies: Gold(III) chloride trihydrate ($HAuCl_4 \cdot 3H_2O$, Beijing Huaxia Ocean Technology Co., Ltd.), sodium hydroxide (NaOH, Aladdin, 96%), sodium citrate dehydrate ($C_6H_5Na_3O_7 \cdot 2H_2O$, Aladdin, 98%), salicylic acid ($C_7H_6O_3$, Aladdin, 99.5%), sodium hypochlorite solution (NaClO, Ailan (Shanghai) Chemical Technology Co., Ltd., available chlorine 14.5%), sodium nitroferricyanide dihydrate ($C_5FeN_6Na_2O \cdot 2H_2O$, Aladdin, 99%), hydrazine monohydrate ($N_2H_4 \cdot H_2O$, >98.0%, Tianjin Sanjiang Technology Co., Ltd.), para-(dimethylamino) benzaldehyde (p-$C_9H_{11}NO$, 99%, Tianjin Sanjiang Technology Co., Ltd.), hydrogen peroxide (H_2O_2, Beijing Chemical Works, 30%), hydrochloric acid (HCl, Tianjin Buohua Chemical Reagent Co., Ltd., 36% to 37%), ammonium chloride (NH_4Cl, Beijing Chemical Works, analytical reagent grade). N_2 gas (≥99.999%) and Ar gas (≥99.99%) were obtained from Huanyu Co., Ltd. All chemicals were used as received without further purification.

Synthesis of ZIF-8

Typically, ZIF-8 was synthesized as follows. A methanolic solution (50 mL) of $Zn(NO_3)_2 \cdot 6H_2O$ (3.6 mmol) was added into a methanolic solution (50 mL) of 2-methylimidazole (28.71 mmol) and kept stirring at room temperature for four hours. The resulting white precipitate was centrifuged and washed several times with methanol before being finally dried in a vacuum at 60 °C for 6 h.

Synthesis of Au_xCu_{1-x} alloys

Au_xCu_{1-x} alloy nanoparticles with various Au/Cu molar ratios were synthesized as follows. Taking $Au_{0.3}Cu_{0.7}$ as an example: First, 35 mL deionized water was added into an

ice-cold 100 mL three-necked round-bottomed flask and stirred under N_2 for 30 min. Second, 0.5 mL $HAuCl_4$ (0.01 g mL^{-1}) and 1.8 mL $CuCl_2$ (0.02 mol L^{-1}) were added into the above solution with continuous stirring for 4 h. Third, 3 mL ice-cold $NaBH_4$ solution (0.01g mL^{-1}) was quickly injected into the flask with magnetic stirring for 4 h. The resultant $AuCu_{3:7}$ product was centrifuged and washed with water and ethanol three times. To obtain other Au_xCu_{1-x} alloy nanoparticles, the Au and Cu atomic ratios could be easily achieved by controlling the amounts of $HAuCl_4$ and $CuCl_2$ precursors.

Synthesis of Au_XCu_{1-X}/ZIF-8

$Au_{0.3}Cu_{0.7}$ nanoparticles supported on ZIF-8 substrate (denoted S3/ZIF-8) were prepared using a procedure similar to the above synthesis of Au_xCu_{1-x} alloy nanoparticles. As a difference, 100 mg of as-prepared ZIF-8 was poured into the mixed solution with magnetic stirring before the third step.

Synthesis of Au/ZIF-8 and Cu/ZIF-8

Au nanoparticles supported on a ZIF-8 substrate (denoted Au/ZIF-8) were synthesized by the similar method to the above Au_3Cu_7/ZIF-8 without the addition of $CuCl_2{\cdot}2H_2O$. Cu nanoparticles supported on a ZIF-8 substrate (denoted Cu/ZIF-8) were also obtained via a similar method to the above S3/ZIF-8, though in the absence of $HAuCl_4{\cdot}3H_2O$.

Characterizations

The structure and crystallinity of the as-synthesized samples were examined via powder X-ray diffraction (PXRD) measurement on Rigaku D/max-2500 X-ray diffractometer using Cu-Kα radiation and a scan step of 4 ° min^{-1} in the range of 5 ° to 90 °. Transmission electron microscopy (TEM, on a JEOL JEM-2800, 200 kV) was used to observe the morphologies of prepared products. X-ray photoelectron spectroscopy (XPS) analysis was performed on a Thermo Scientific ESCALAB 250 Xi spectrometer equipped

with a monochromatic Al Kα X-ray source (1486.6 eV). The metal mass loading of Au and Cu in the as-synthesized composites was determined via inductively coupled plasma/atomic emission spectroscopy (ICP-AES). Gaseous N_2 adsorption-desorption isotherms were recorded on a Quantachrome Nova 2000e sorption analyzer at liquid nitrogen temperature (77 K). Specific surface areas were evaluated by using the multi-point Brunauer-Emmett-Teller (BET) method and pore size distributions were determined from the adsorption branch using the non-local density functional theory (NLDFT) method. UV-Vis absorbance data were obtained on a KU-T1810 ultraviolet-visible (UV-Vis) spectrophotometer. The electrochemical *in situ* Fourier transform infrared (*in situ* FTIR) spectroscopy was tested using a Nexus 870 spectrometer (Nicolet) equipped with a liquid-nitrogen-cooled MCT-A detector and an EverGlo IR source. *In situ* FTIR spectra were recorded by means of time-resolved FTIR spectroscopy procedures. The resulting spectra were reported as the relative change in reflectivity and calculated as follows:

$$\frac{\Delta R}{R} = \frac{R(E_S) - R(E_R)}{R(E_R)}$$

where $R(E_S)$ and $R(E_R)$ are the accumulated spectra collected at sample potential E_S and reference potential E_R, respectively.

Electrochemical measurements

Electrochemical performance measurements were carried out on a WaveDrive 20 Bipotentiostat/Galvanostat (Pine Research Instrumentation, USA) with a three-electrode system in a two-compartment cell separated by a Nafion 211 membrane. A carbon-paper electrode, loaded with catalyst, was used as the working electrode, with a graphitic rod and Ag/AgCl electrode being used as the counter and reference electrodes, respectively. All potentials in this study were calibrated to the reversible hydrogen electrode (RHE) according to the equation: $E_{vs\ \mathrm{RHE}} = E_{vs\ \mathrm{Ag/AgCl}} + 0.059\ \mathrm{pH} + E^{o}_{\mathrm{Ag/AgCl}}$. All tests were performed at room temperature. For N_2 reduction reaction (NRR) experiments, the

electrolyte (0.1 M HCl, 0.1 M Na_2SO_4 or 0.1 M KOH) was bubbled with N_2 for 0.5 h before measurement. The N_2 gas (≥99.999%), Ar gas (≥99.99%) and compressed air used in this experiment were pre-purified through flowing into alkaline solution (pH=13 KOH aqueous solution) and acid solution (pH=1 H_2SO_4 aqueous solution) to remove any N contamination in the N_2 before entering the electrolyte solution. The presented current densities refer to a geometric surface area of 1 × 1 cm^2 on carbon paper.

Determination of NH_3

Concentrations of NH_3 were spectrophotometrically determined via the indophenol blue method. Briefly, a 2 mL aliquot of the electrolyte solution was pipetted from the electrochemical reaction vessel and added into 2 mL of 1 M NaOH solution containing 5 wt% salicylic acid and 5 wt% sodium citrate. Subsequently, 1 mL of 0.05 M NaClO and 0.2 mL of 1 wt% $C_5FeN_6Na_2O$ were also added into the above solution. After aging at room temperature for 2 h, the UV-Vis absorption spectrum was measured. The concentration of indophenol blue was determined using absorbance at a wavelength of 655 nm. The fitting curve ($y = 0.365x + 0.004$, $R^2 = 0.999$) consistently showed a strong linear relationship between the absorbance value and NH_3 concentration throughout three independent calibrations.

Determination of N_2H_4

The concentration of N_2H_4 in the electrolyte was estimated via the Watt and Chrisp method. A colored reagent was first obtained by mixing the p-$C_9H_{11}NO$ (5.99 g), HCl (30 mL) and C_2H_5OH (300 mL). Subsequently, 5 mL of electrolyte was collected from the electrochemical reaction vessel, added into 5 mL of the as-prepared color reagent and stirred for 10 min at 25 °C. The absorbance of the resulting solution was measured at 455 nm. The fitting curve ($y = 0.563x + 0.014$, $R^2 = 0.999$) showed a strong linear relationship

between the absorbance value and N_2H_4 concentration throughout three independent calibrations.

Faradaic efficiency

The ammonia formation rate was first calculated using the equation: $v_{NH3} = (C_{NH3} \times V)/(t \times m)$, where C_{NH3} is the measured NH_3 concentration, V is the volume of the HCl electrolyte, t is the reduction reaction time and m is the loading mass of the Au_xCu_{1-x} catalyst. Faradaic efficiency (FE) was calculated according to equation: $FE = 3F \times n_{NH3}/Q$, where F is the Faraday constant and Q is the quantity of applied electricity.

Isotope Labeling Experiments

The ^{14}N and ^{15}N isotopic labeling experiments were performed using $^{14}N_2$ and $^{15}N_2$ as the feeding gases (99% enrichment of ^{15}N in $^{15}N_2$, supplied by Beijing Yinuokai Technology Co., Ltd.). Each NRR experiment was conducted at -0.2 V (vs. RHE) for 2.5 h. Then, 0.5 mL of above solution mixed with 0.05 mL of d6-DMSO was used for ^{1}H nuclear magnetic resonance (NMR) spectroscopy measurement (Bruker AVANCE III 600 MHz). The corresponding absolute calibration curves were recorded by using the $^{15}NH_4Cl$ (99% isotopic purity, Shanghai Xinbo Chemical Technology Co., Ltd.) and $^{14}NH_4Cl$ aqueous solutions with a series of known concentrations as the standards.

Calculation details

This study used the Vienna *ab initio* simulation package (VASP)[1, 2] to perform periodic, self-consistent density functional theory (DFT) calculations. The generalized gradient approximation (GGA) in the form of Perdew-Burke-Ernzerhof (PBE)[3] was used to calculate the electronic structures. The inner cores were described by the project-augment wave

(PAW) scheme.[4, 5] The electronic wave functions were expanded on a plane wave basis, where the kinetic cut-off energy was 400 eV.

A vacuum region of 15 Å was used to avoid the interaction between two adjacent slabs. The Brillouin-zone integrations were performed using a 3×3×1 Monkhorst-Pack grid, which was tested and found to be a reasonable choice for these calculations.[6] During the calculations, the upper two layers and any adsorbed species were allowed to be relaxed until the residual force on each atom was smaller than 0.035 eV $Å^{-1}$.

The Gibbs free energy change (ΔG) at 298.15 K for each elemental step was calculated by the formula: $\Delta G = \Delta E + \Delta E_{ZPE} - T\Delta S$, where ΔE is the electronic energy difference of one given step, ΔE_{ZPE} and ΔS are the changes in zero point energies and entropy, respectively, and only vibrational entropy was considered for a surface reaction step, as seen in **Table S2** and based on the formula: $S_{vib} = R\sum_{i}^{\#of\ \mathrm{modes}}\left[\frac{x_i}{e^{x_i}-1} - \ln(1-e^{-x_i})\right], x_i = \frac{h\nu_i}{k_B T}$ [7].

Figures and Tables

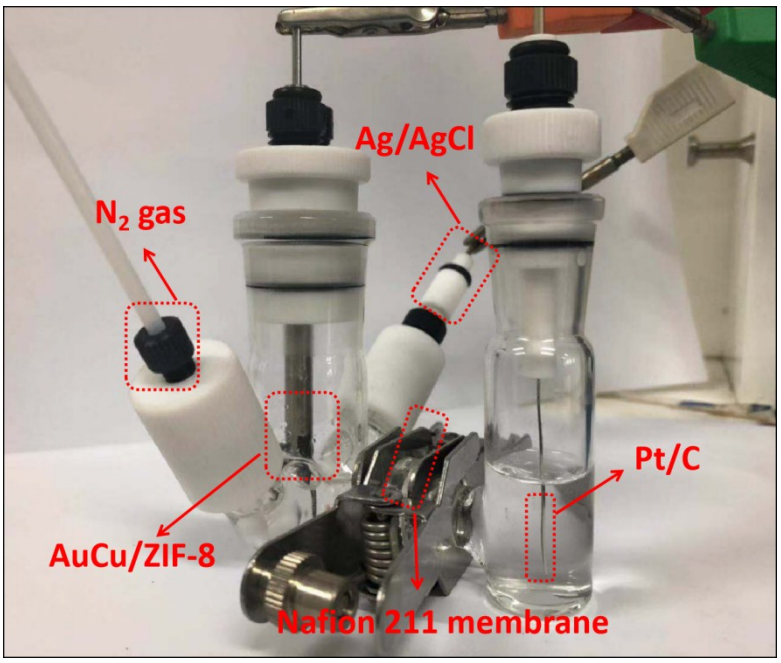

Fig. S1 Optical photograph of electrocatalytic NRR process using the three-electrode glass cell.

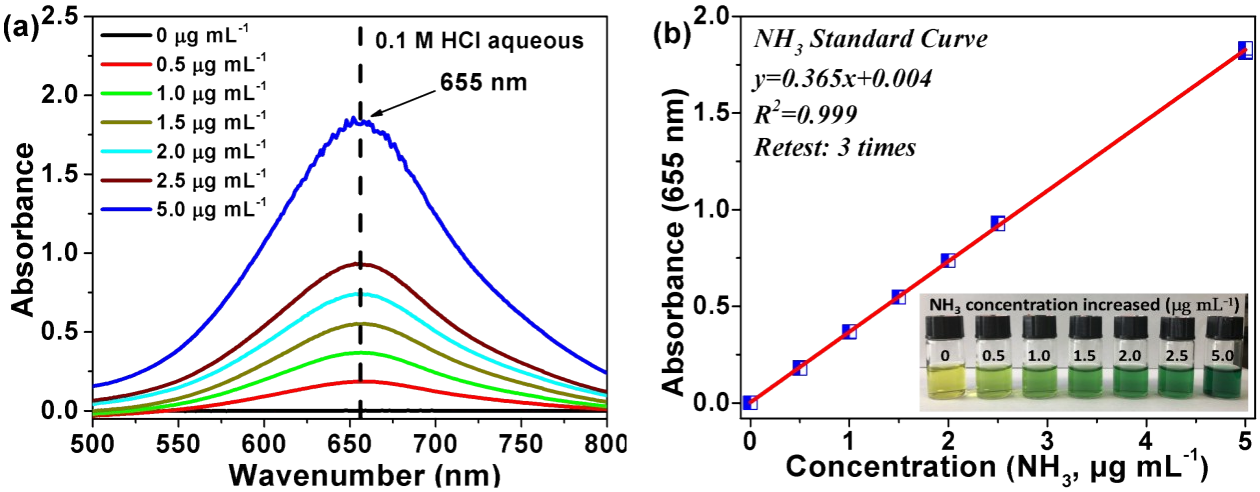

Fig. S2 (a) UV-Vis absorption curves and (b) corresponding calibration curve of indophenol assays with NH_3 at 655 nm after incubating for 2 h at room temperature in 0.1 M HCl.

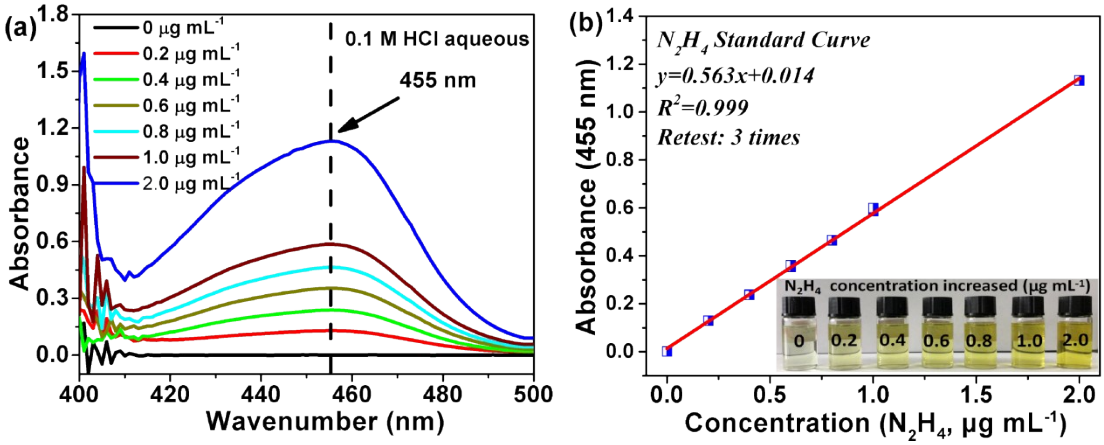

Fig. S3 (a) UV-Vis absorption curves and (b) the corresponding calibration curve of various N_2H_4 concentrations at 455 nm after incubating for 30 min at room temperature in 0.1 M HCl.

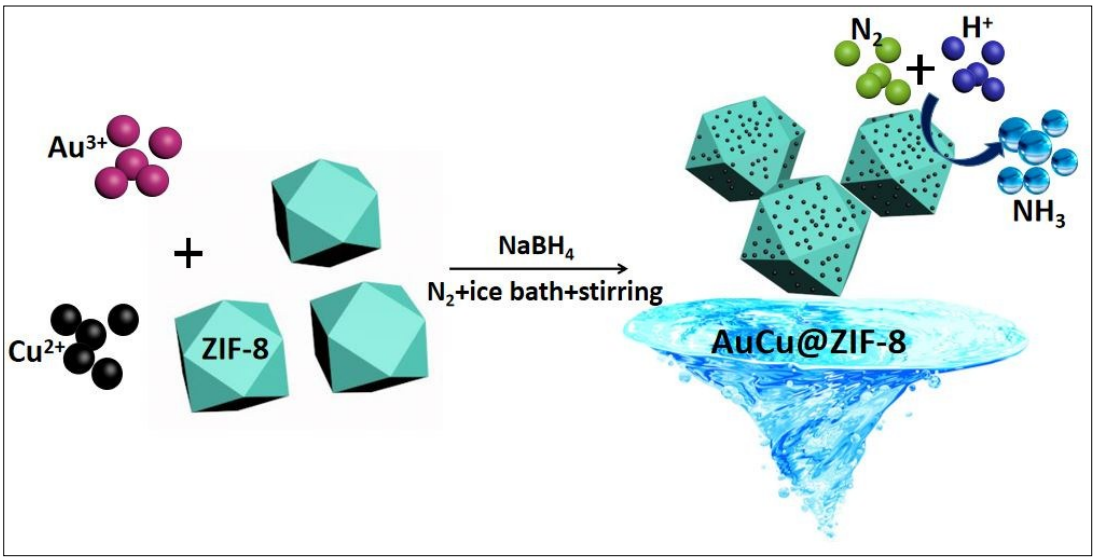

Fig. S4 Schematic illustration of the AuCu/ZIF-8 synthesis.

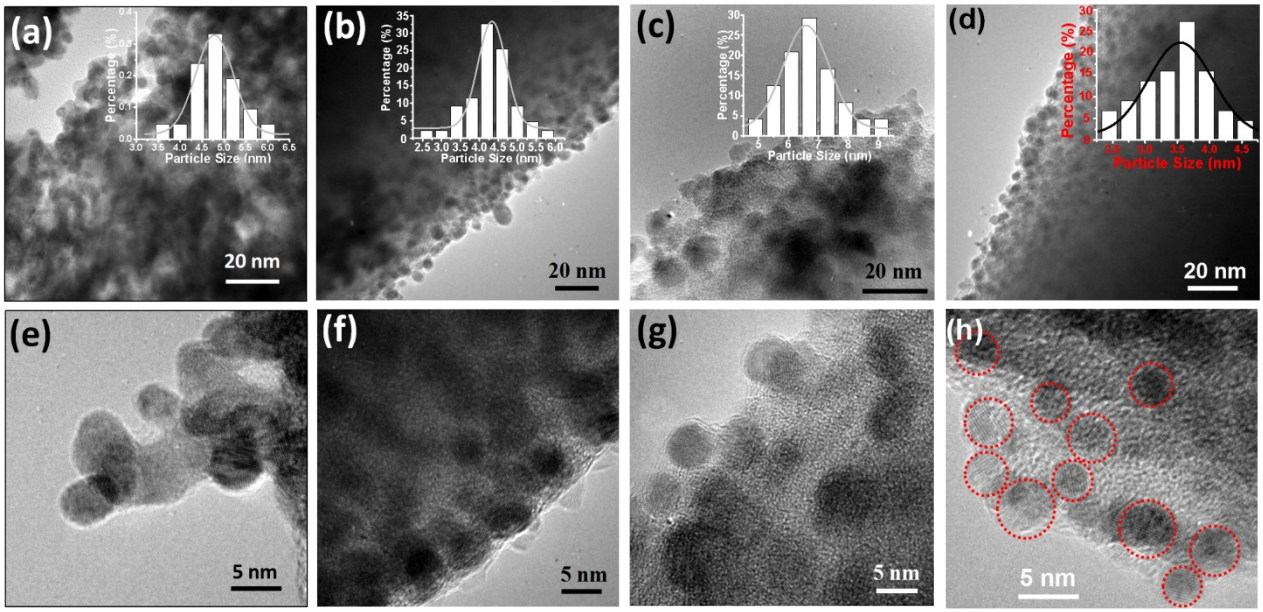

Fig. S5 TEM images of (a) and (e) S3, (b) and (f) Au/ZIF-8, (c) and (g) Cu/ZIF-8, (d) and (h) S3/ZIF-8.

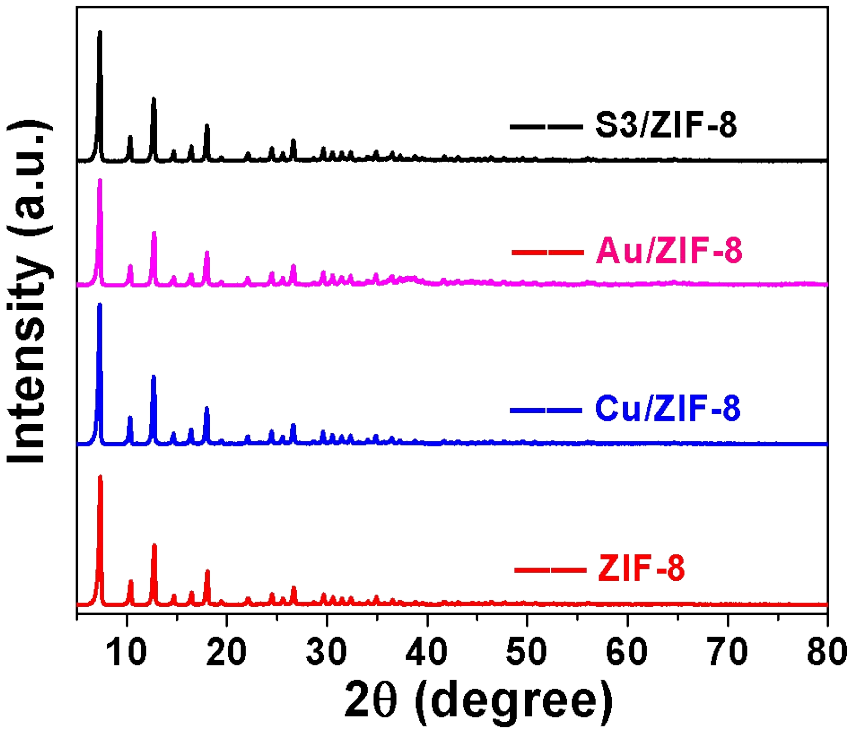

Fig. S6 XRD patterns for S3/ZIF-8, Au/ZIF-8, Cu/ZIF-8 and ZIF-8.

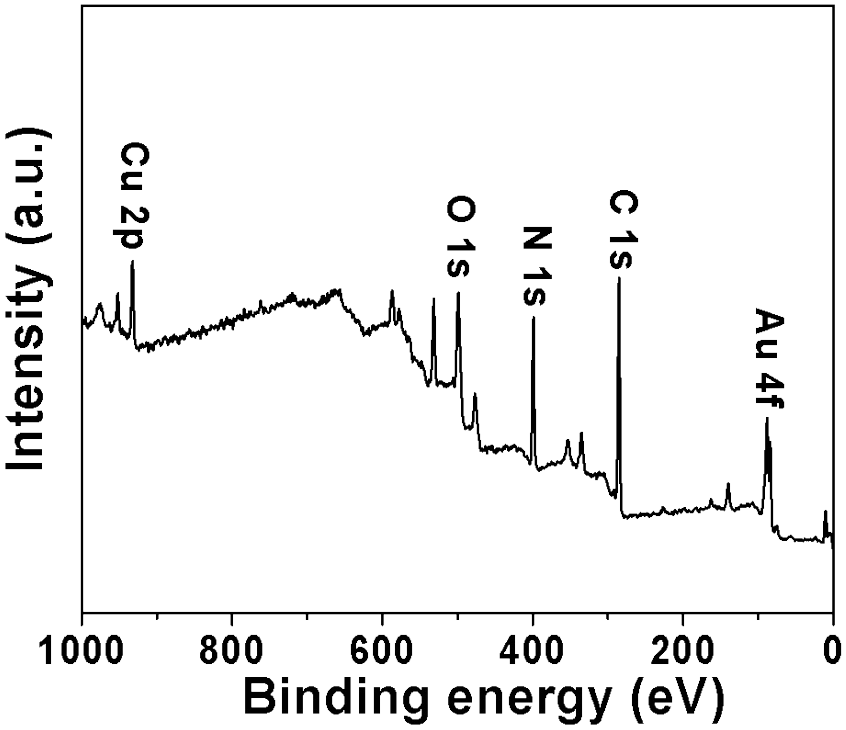

Fig. S7 XPS survey spectrum of S3/ZIF-8.

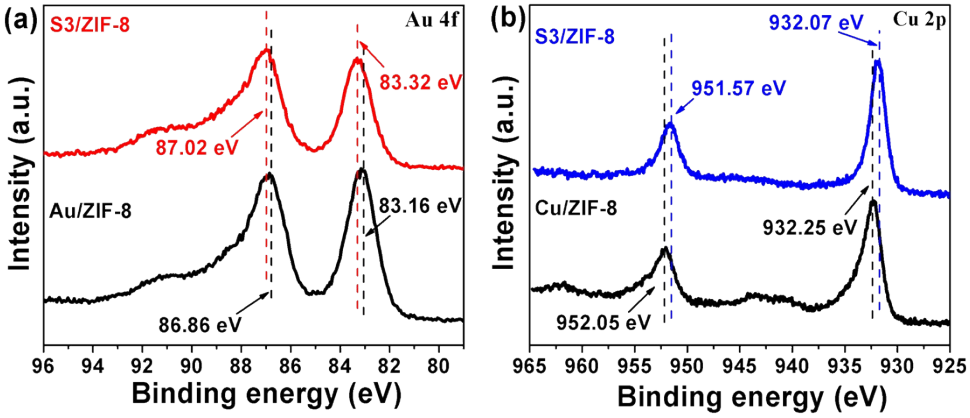

Fig. S8 High resolution XPS spectra of (a) Au 4f of S3/ZIF-8 and Au/ZIF-8, and (b) Cu 2p of S3/ZIF-8 and Cu/ZIF-8.

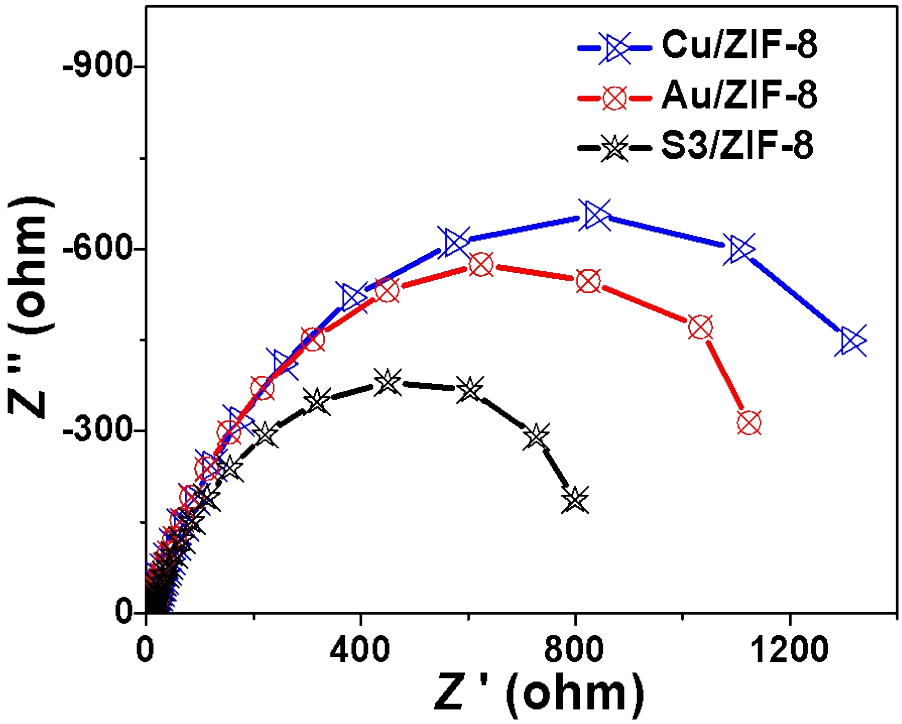

Fig. S9 Nyquist plots of S3/ZIF-8, Au/ZIF-8 and Cu/ZIF-8 on carbon paper in 0.1 M HCl.

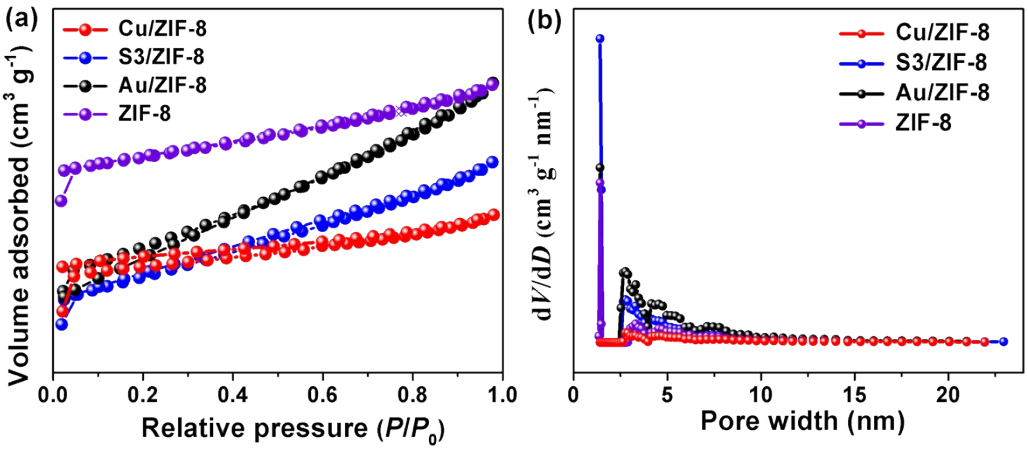

Fig. S10 (a) N_2 adsorption-desorption isotherms and (b) corresponding pore size distribution curves of ZIF-8, S3/ZIF-8, Au/ZIF-8 and Cu/ZIF-8. The specific surface area (S_{BET}) values of S3/ZIF-8, Cu/ZIF-8, Au/ZIF-8 and ZIF-8 are 946, 945, 1057 and 1313 m^2 g^{-1}, respectively.

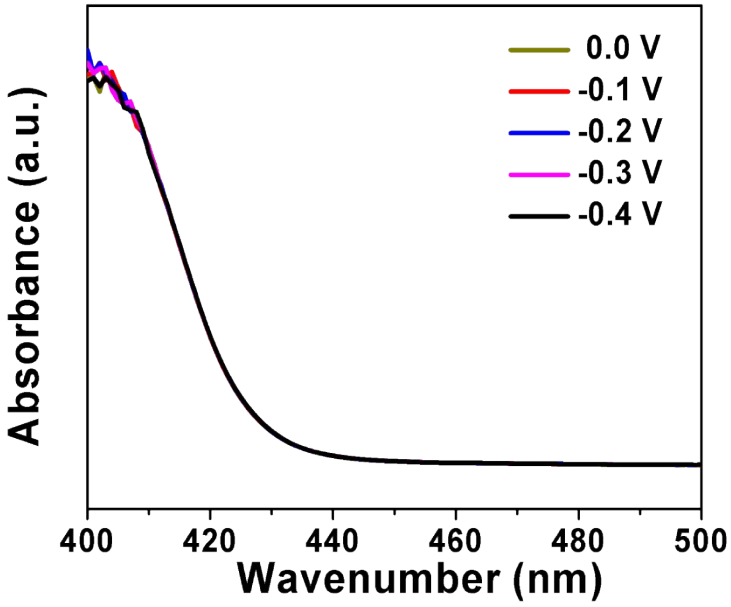

Fig. S11 UV-Vis absorption spectra of the electrolytes (0.1 M HCl) estimated by the method of Watt and Chrisp after NRR electrolysis at different potentials.

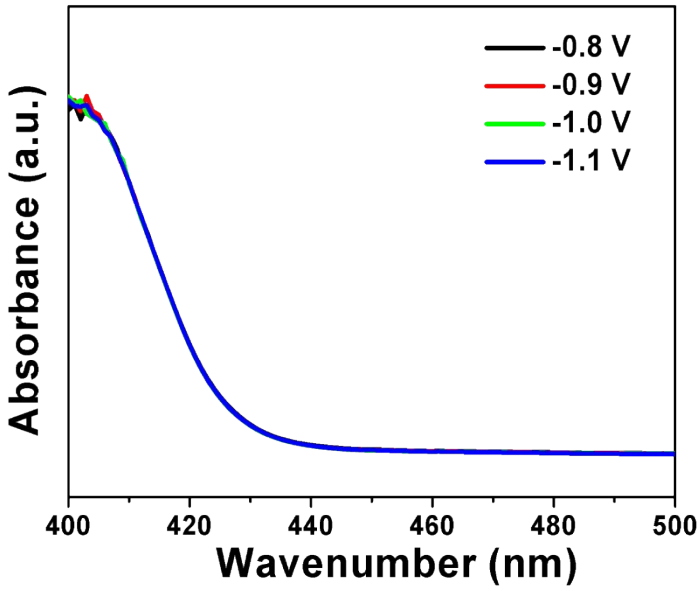

Fig. S12 UV-Vis absorption spectra of the electrolytes (0.1 M Na_2SO_4) estimated by the method of Watt and Chrisp after NRR electrolysis at different potentials.

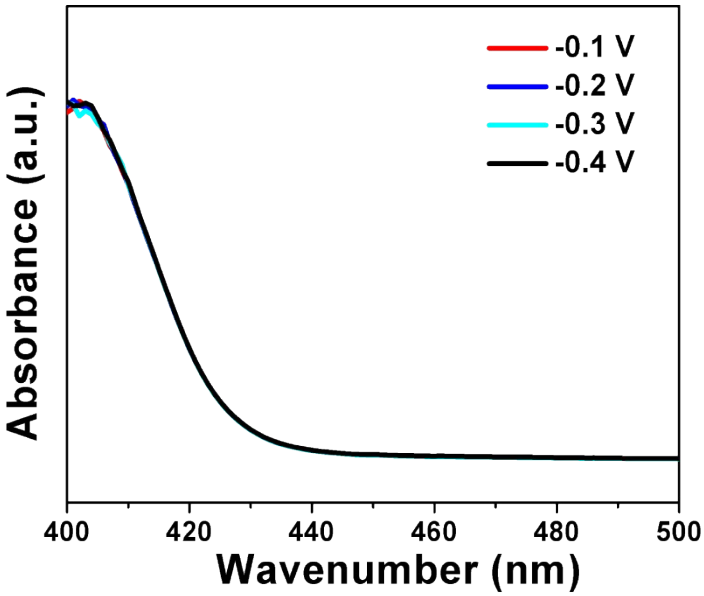

Fig. S13 UV-Vis absorption spectra of the electrolytes (0.1 M KOH) estimated by the method of Watt and Chrisp after NRR electrolysis at different potentials.

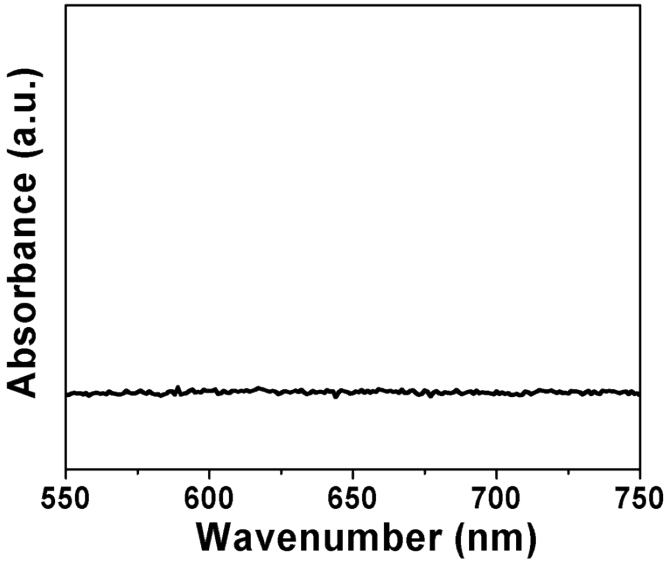

Fig. S14 UV-Vis absorption spectra of the HCl electrolyte stained with indophenol indicator after charging the S3/ZIF-8 electrode in Ar-bubbled 0.1 M HCl for 2.5 h.

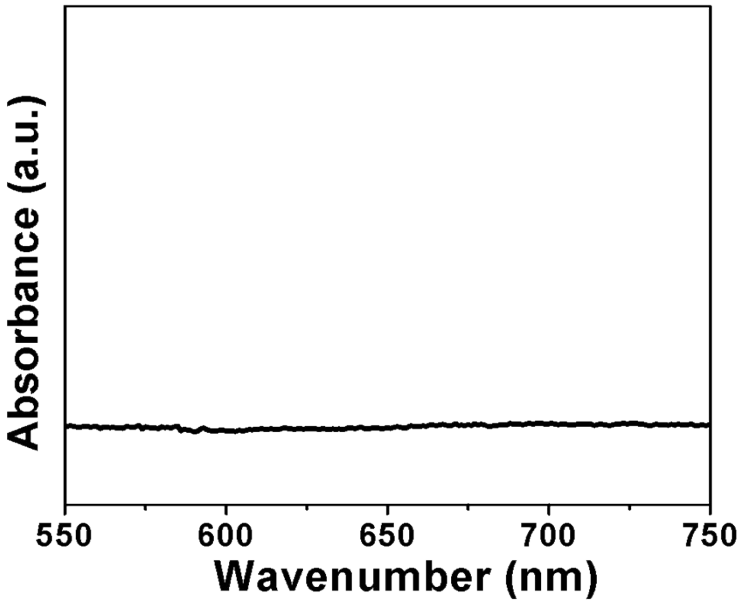

Fig. S15 UV-Vis absorption spectra of the HCl electrolyte stained with indophenol indicator after charging the S3/ZIF-8 electrode in N_2-bubbled 0.1 M HCl at open-circuit potential for 2.5 h.

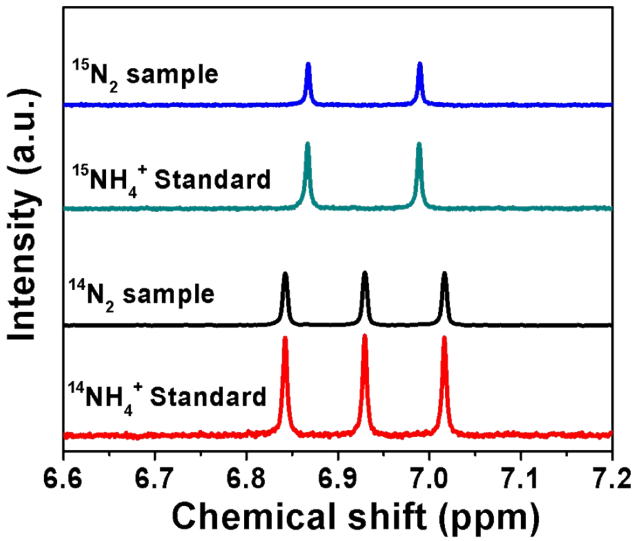

Fig. S16 ^1H NMR spectra of both $^{14}NH^{4+}$ and $^{15}NH^{4+}$ produced from the NRR reaction using $^{14}N_2$ and $^{15}N_2$ as the feeding gases for S3/ZIF-8.

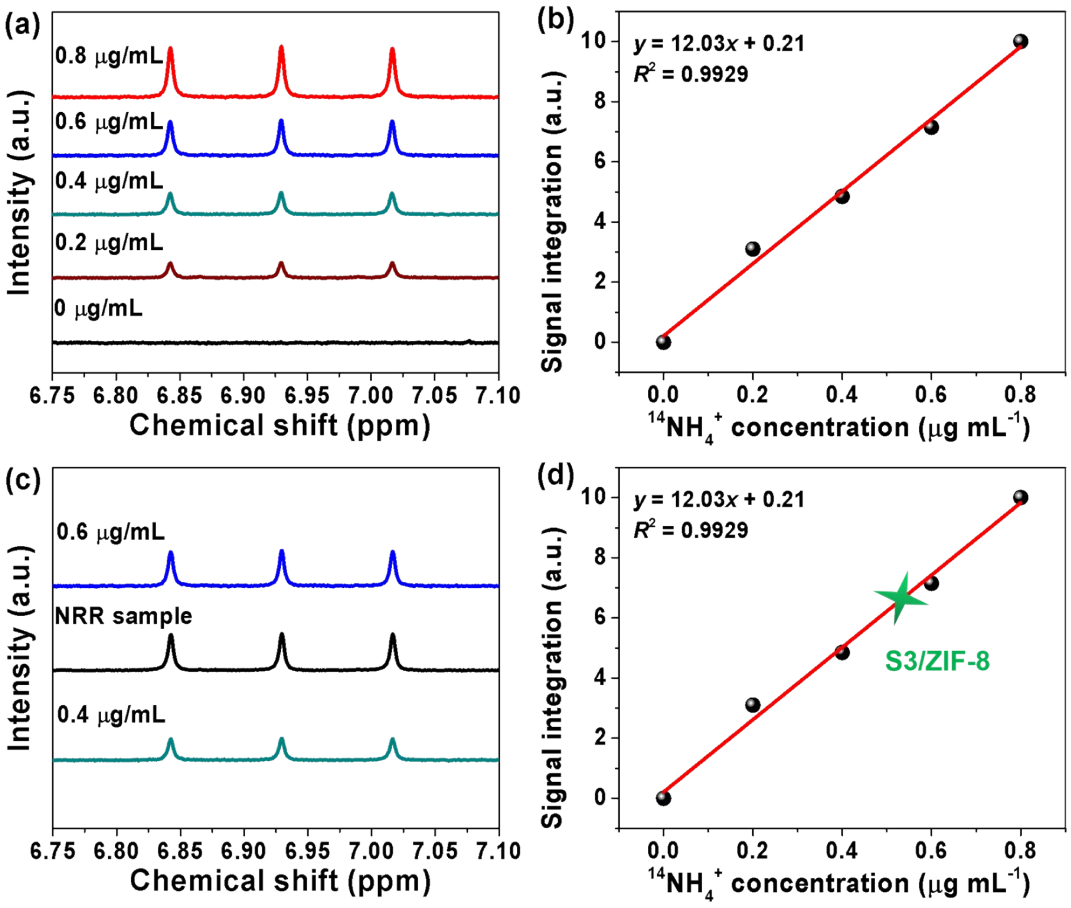

Fig. S17 (a) ^{1}H NMR spectra of $^{14}NH_4^+$ standard samples with different concentrations. (b) The corresponding calibration curve of $^{14}NH_4^+$ concentration vs. peak area intensity of NMR spectra. (c) ^{1}H NMR spectra of the electrolyte after catalyzing on S3/ZIF-8 at -0.2 V (vs. RHE) for 2.5 h (black) and $^{14}NH_4^+$ standard samples with 0.4 μg mL^{-1} (green) and 0.6 μg mL^{-1}(blue). (d) The $^{14}NH_4^+$ concentration of the electrolyte after catalyzing on S3/ZIF-8 at -0.2 V (vs. RHE) for 2.5 h (green star), quantitatively determined by the above $^{14}NH_4^+$ calibration curve.

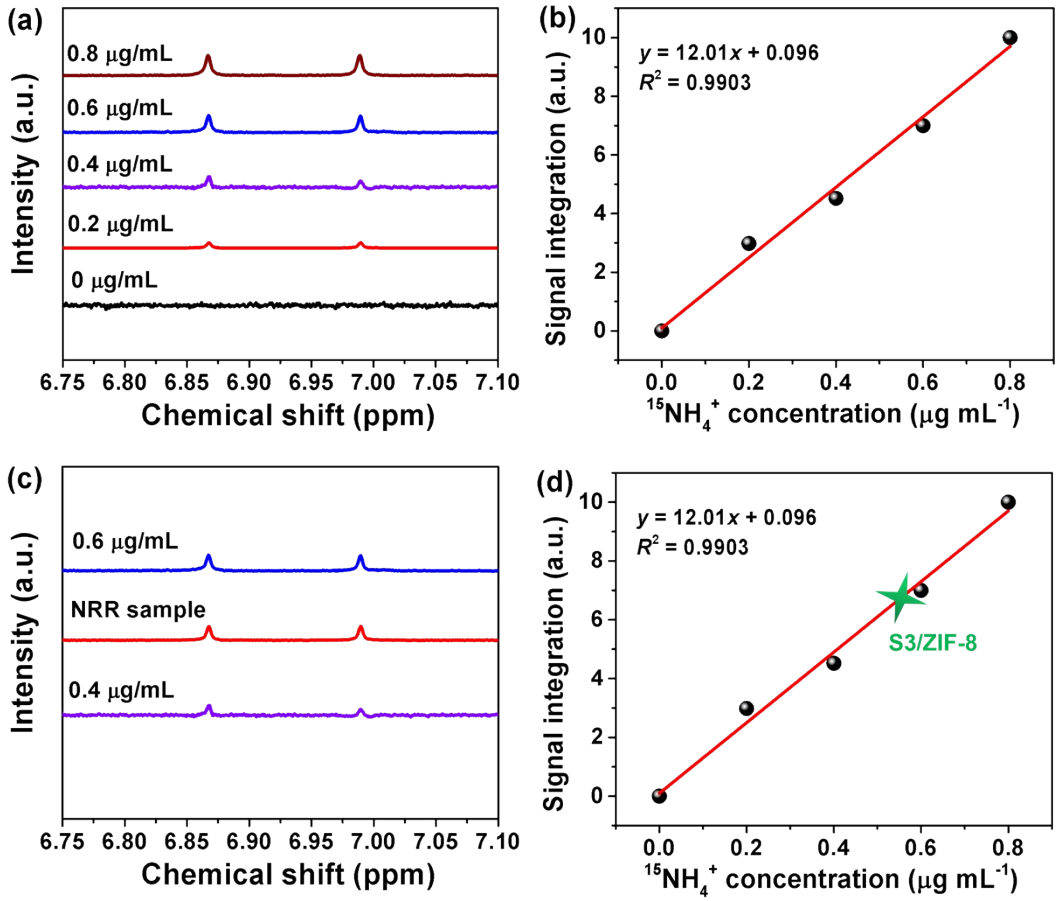

Fig. S18 (a) ^{1}H NMR spectra of $^{15}NH_4^+$ standard samples with different concentrations. (b) The corresponding calibration curve of $^{15}NH_4^+$ concentration vs. peak area intensity of NMR spectra. (c) NMR spectra of the electrolyte after catalyzing on S3/ZIF-8 at -0.2 V (vs. RHE) for 2.5 h (red) and $^{15}NH_4^+$ standard samples with 0.4 μg mL^{-1} (purple) and 0.6 μg mL^{-1} (blue). (d) The $^{15}NH_4^+$ concentration of the electrolyte after catalyzing on S3/ZIF-8 at -0.2 V (vs. RHE) for 2.5 h (green star), quantitatively determined by the above $^{15}NH^{4+}$ calibration curve.

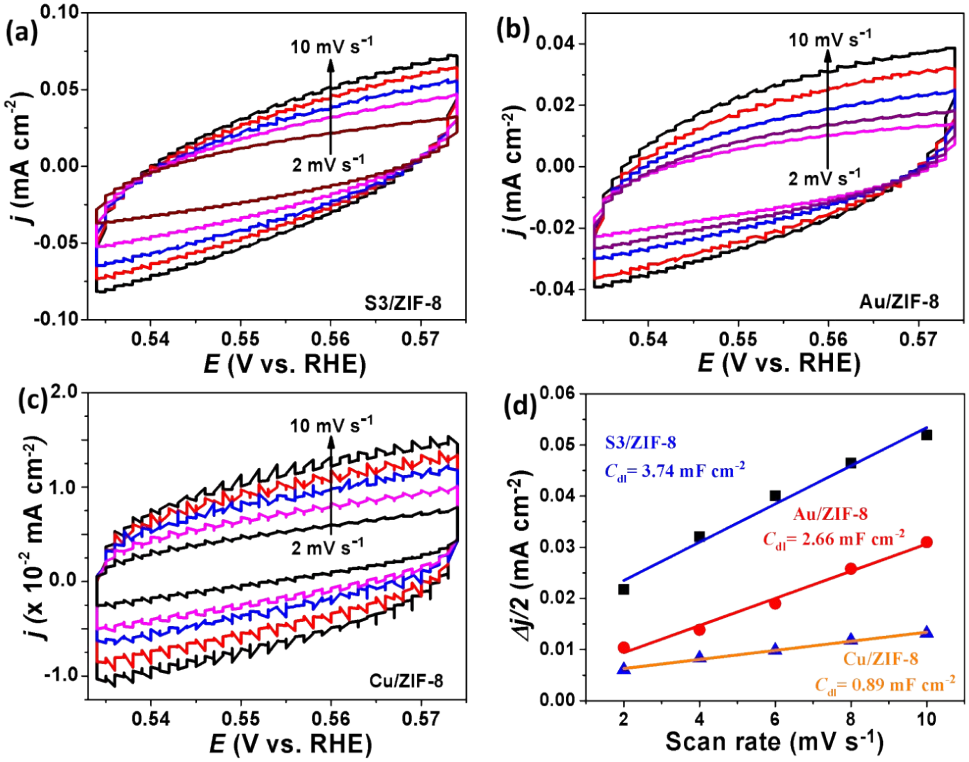

Fig. S19 Cyclic voltammograms of (a) S3/ZIF-8, (b) Au/ZIF-8 and (c) Cu/ZIF-8 on carbon paper and measured at different scan rates from 2 to 10 mV s^{-1}. (d) The corresponding plots of current density at 0.56 V versus the scan rate.

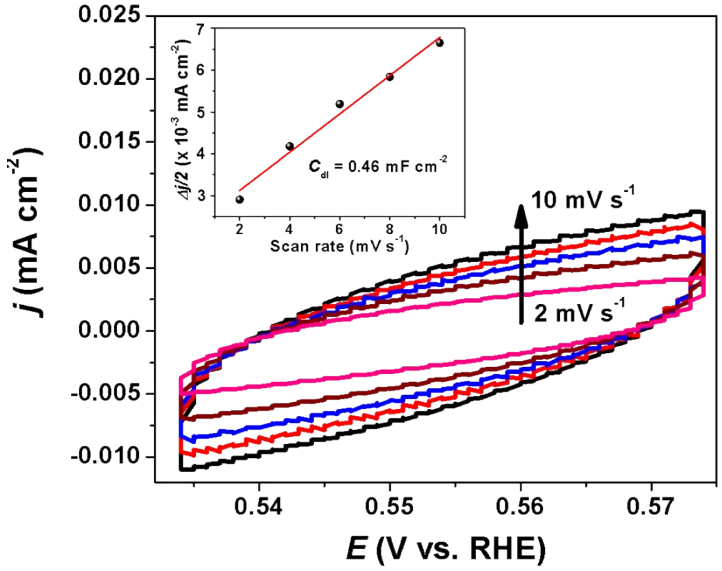

Fig. S20 Cyclic voltammograms of AuCu on carbon paper measured at different scan rates from 2 to 10 mV s^{-1}. Inset: the corresponding plot of current density at 0.56 V versus the scan rate.

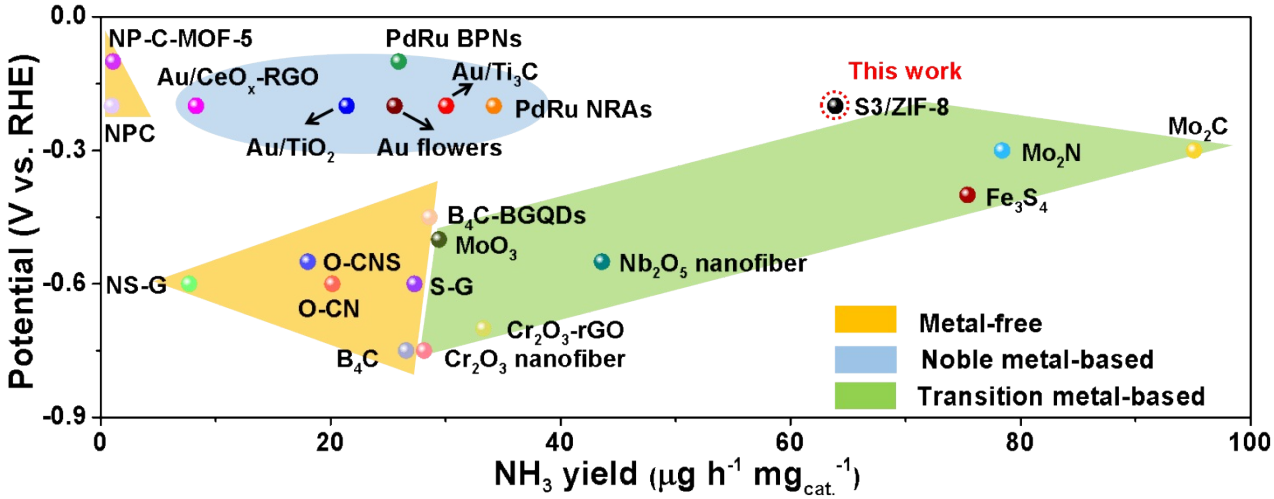

Fig. S21 Comparison of the NRR performance to state-of-the-art catalysts.

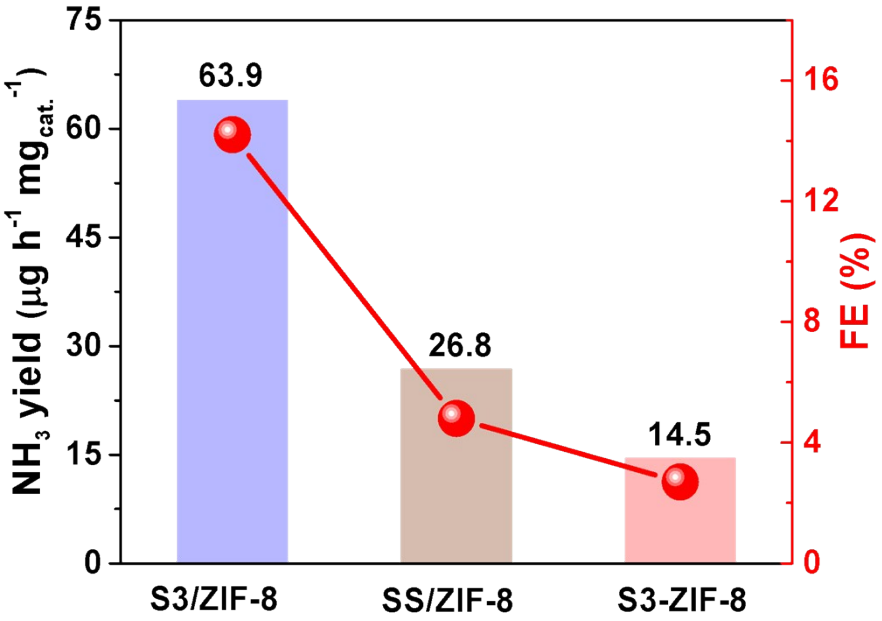

Fig. S22 Maximum NH_3 yields and FEs for S3/ZIF-8, SS/ZIF-8 and S3-ZIF-8 in 0.1 M HCl at room temperature and under ambient pressure.

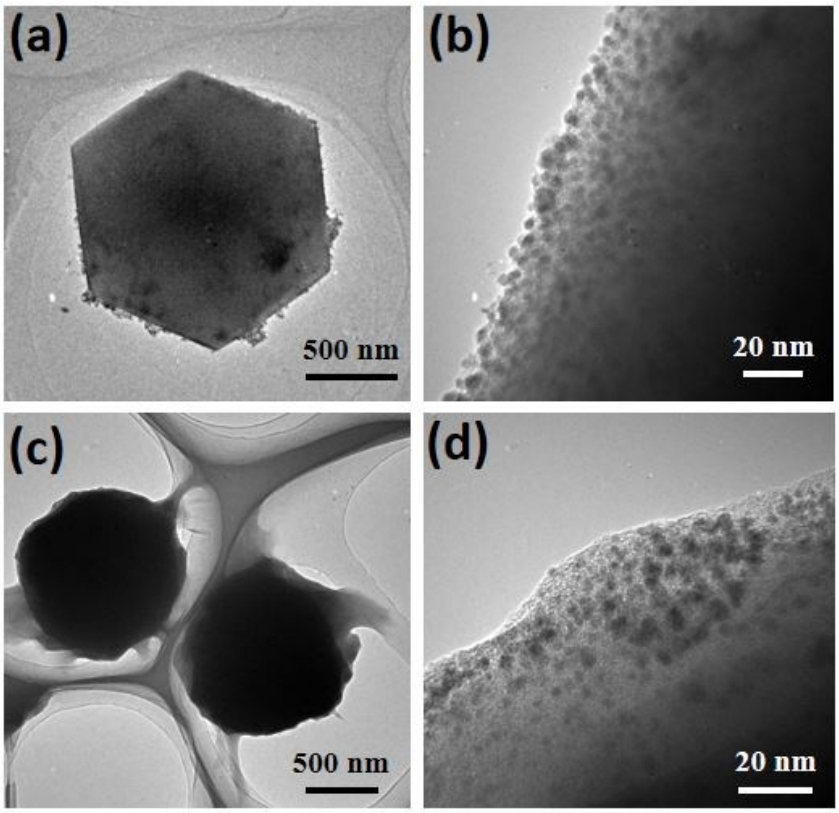

Fig. S23 TEM images of S3/ZIF-8 (a, b) before and after (c, d) NRR tests in 0.1 M HCl.

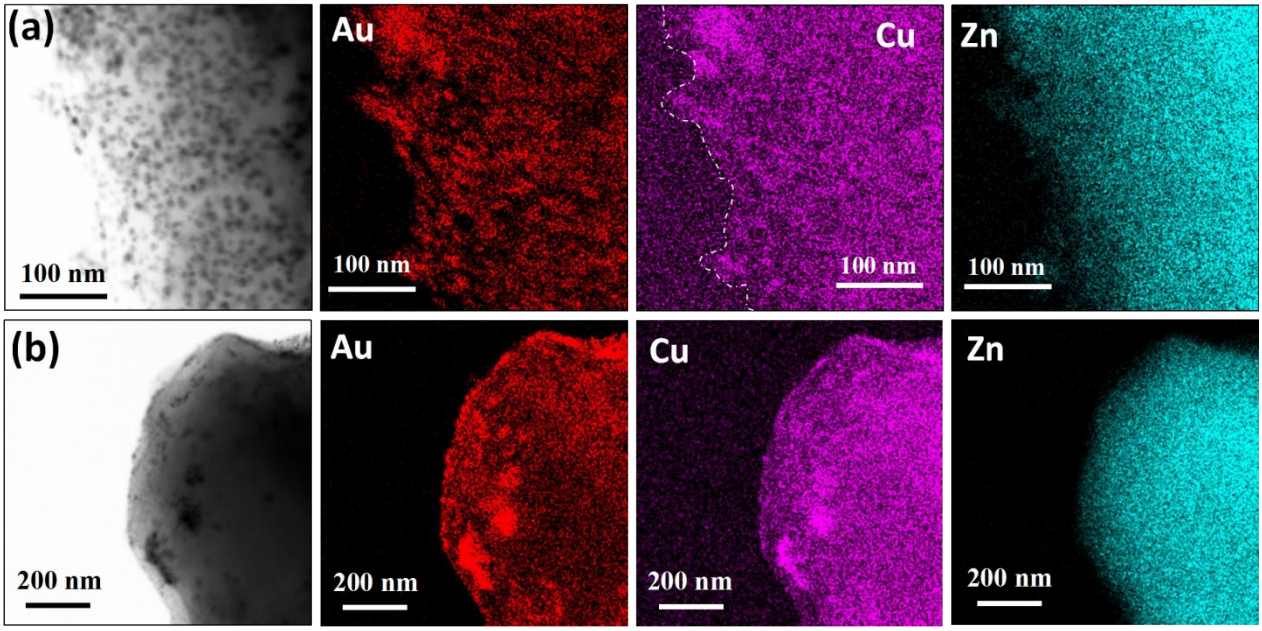

Fig. S24 STEM images and the corresponding STEM-EDX mapping images of S3/ZIF-8 before (a) and after (b) NRR tests in 0.1 M HCl.

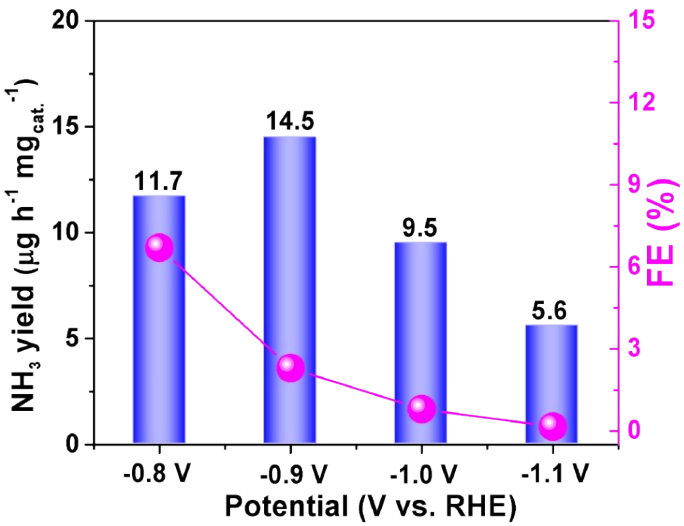

Fig. S25 NH_3 yield rates and FEs for S3/ZIF-8 under different potentials in N_2-bubbled 0.1 M Na_2SO_4.

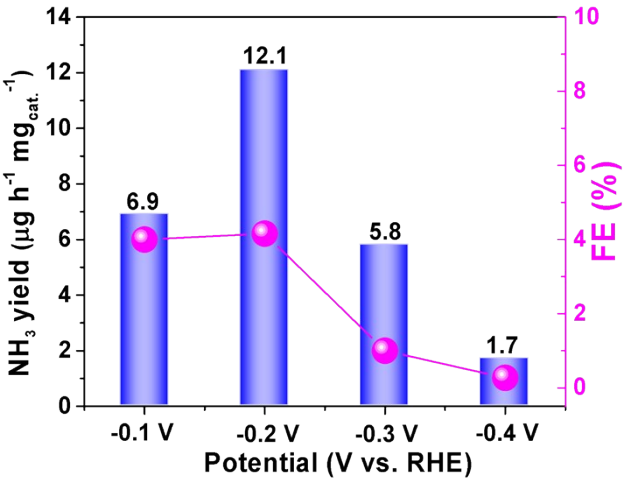

Fig. S26 NH_3 yield rates and FEs for S3/ZIF-8 under different potentials in N_2-bubbled 0.1 M KOH.

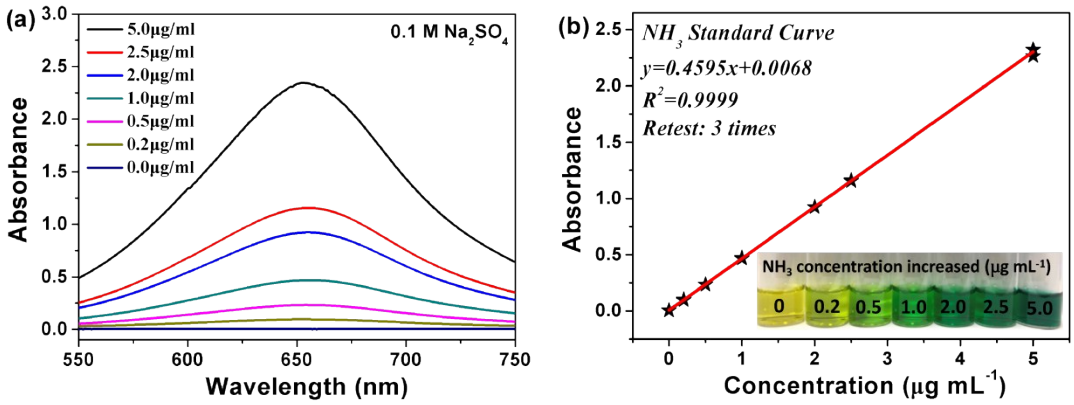

Fig. S27 (a) UV-Vis absorption curves and (b) corresponding calibration curve of indophenol assays with NH_3 after incubating for 2 h at room temperature in 0.1 M Na_2SO_4.

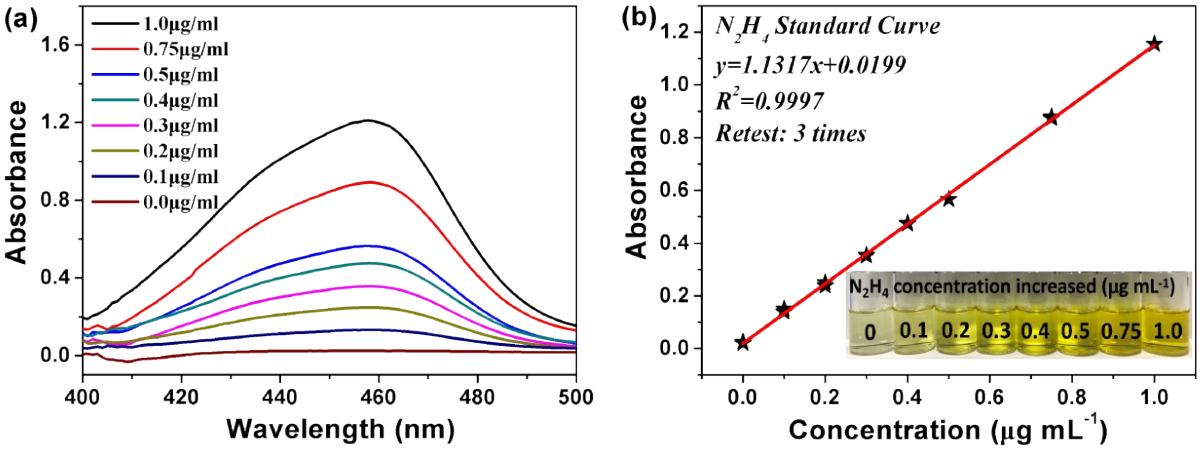

Fig. S28 (a) UV-Vis absorption curves and (b) the corresponding calibration curve of various N_2H_4 concentrations after incubating for 30 min at room temperature in 0.1 M Na_2SO_4.

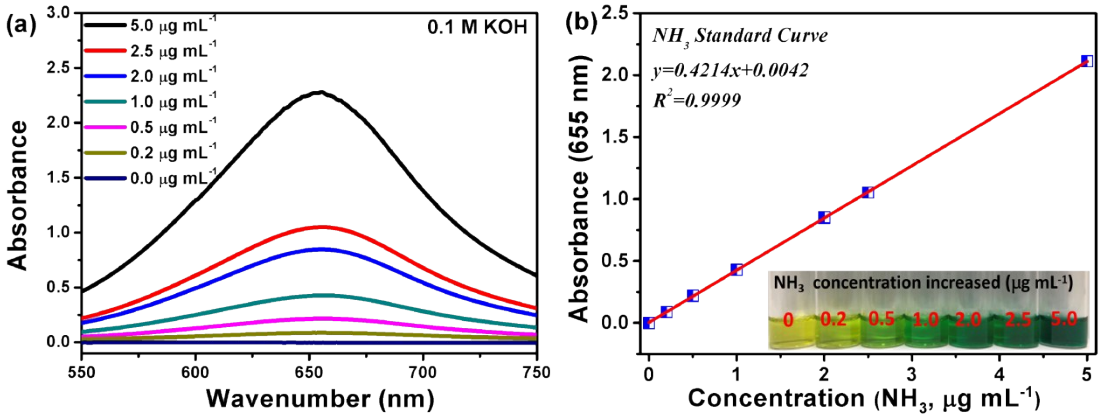

Fig. S29 (a) UV-Vis absorption curves and (b) the corresponding calibration curve of indophenol assays with NH_3 after incubating for 2 h at room temperature in 0.1 M KOH.

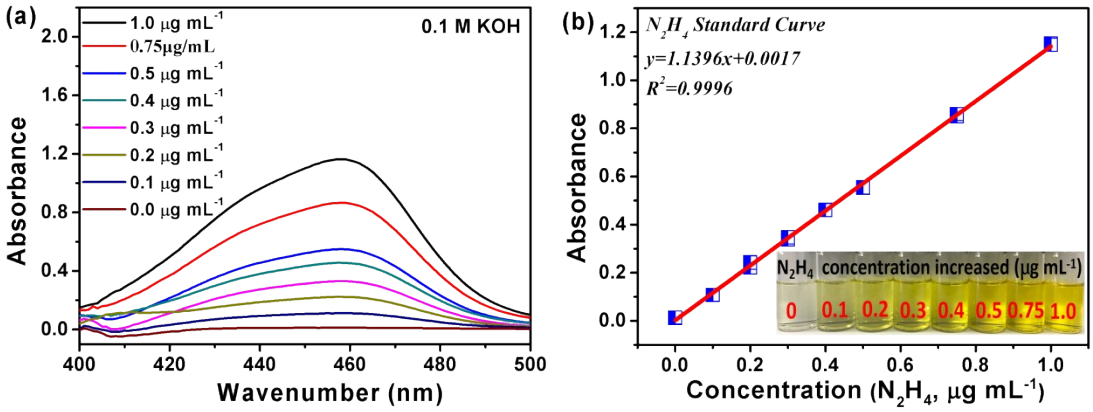

Fig. S30 (a) UV-Vis absorption curves and (b) the corresponding calibration curve of various N_2H_4 concentration after incubating for 30 min at room temperature in 0.1 M KOH.

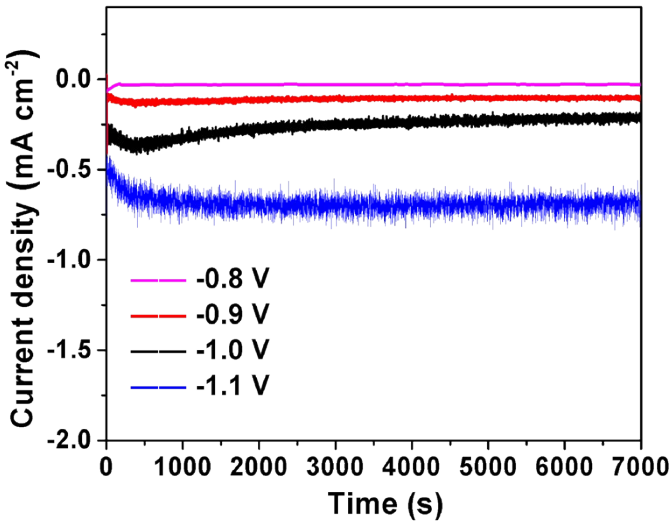

Fig. S31 Time-dependent current density curves for S3/ZIF-8 at different potentials in N_2-bubbled 0.1 M Na_2SO_4.

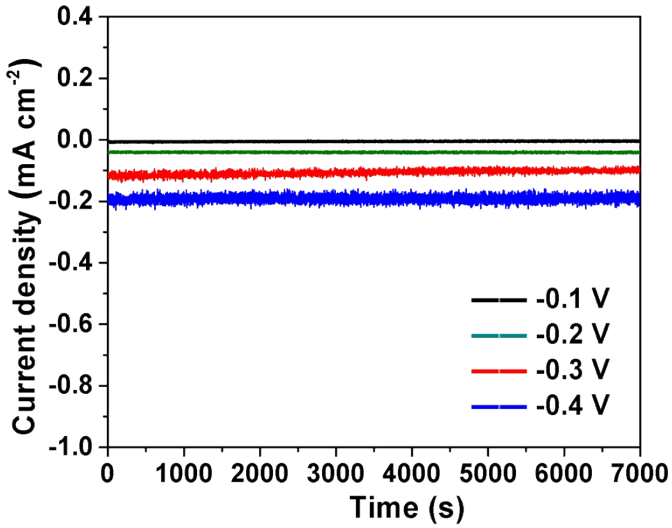

Fig. S32 Time-dependent current density curves for S3/ZIF-8 at different potentials in N_2-bubbled 0.1 M KOH.

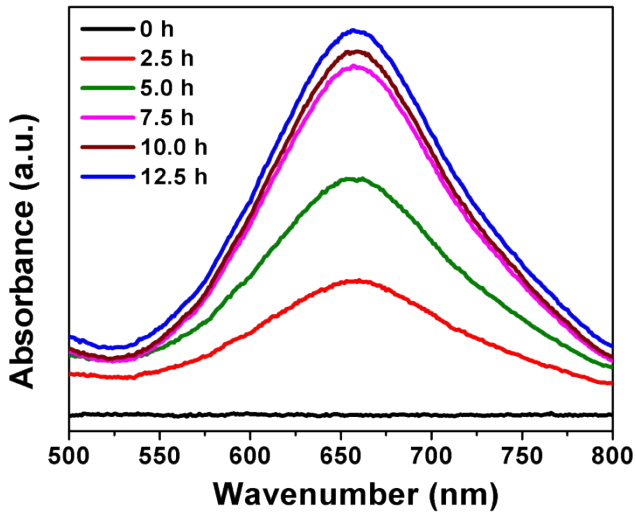

Fig. S33 UV-Vis absorption curves of S3/ZIF-8 at -0.2 V vs RHE. All experiments were performed in air-bubbled 0.1 M HCl at room temperature and under ambient pressure.

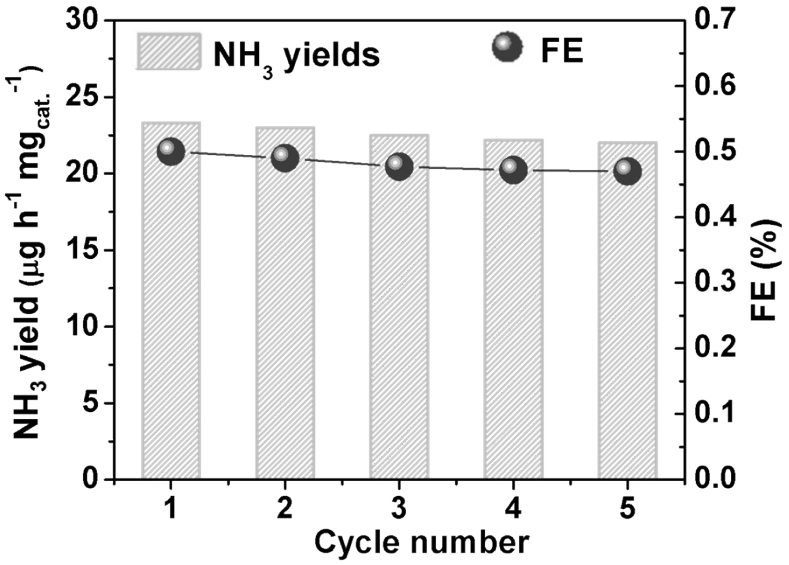

Fig. S34 Recycling tests of S3/ZIF-8 in air-bubbled 0.1 M HCl at the potential of -0.2 V vs. RHE.

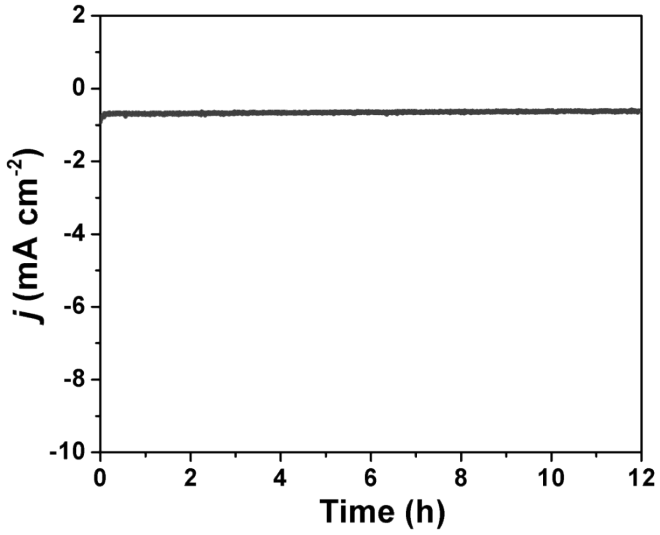

Fig. S35 Chronoamperometry curve of S3/ZIF-8 in air-bubbled 0.1 M HCl at a fixed overpotential of -0.2 V for 12 h.

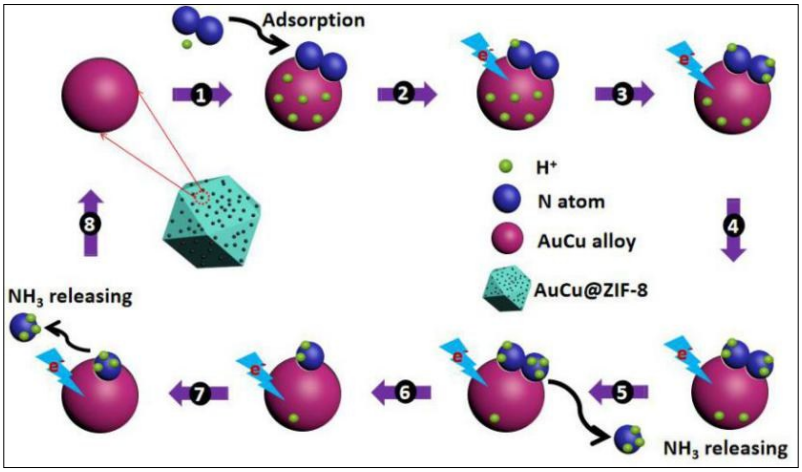

Fig. S36 The proposed pathway for the NH_3 synthesis using S3/ZIF-8 catalyst.

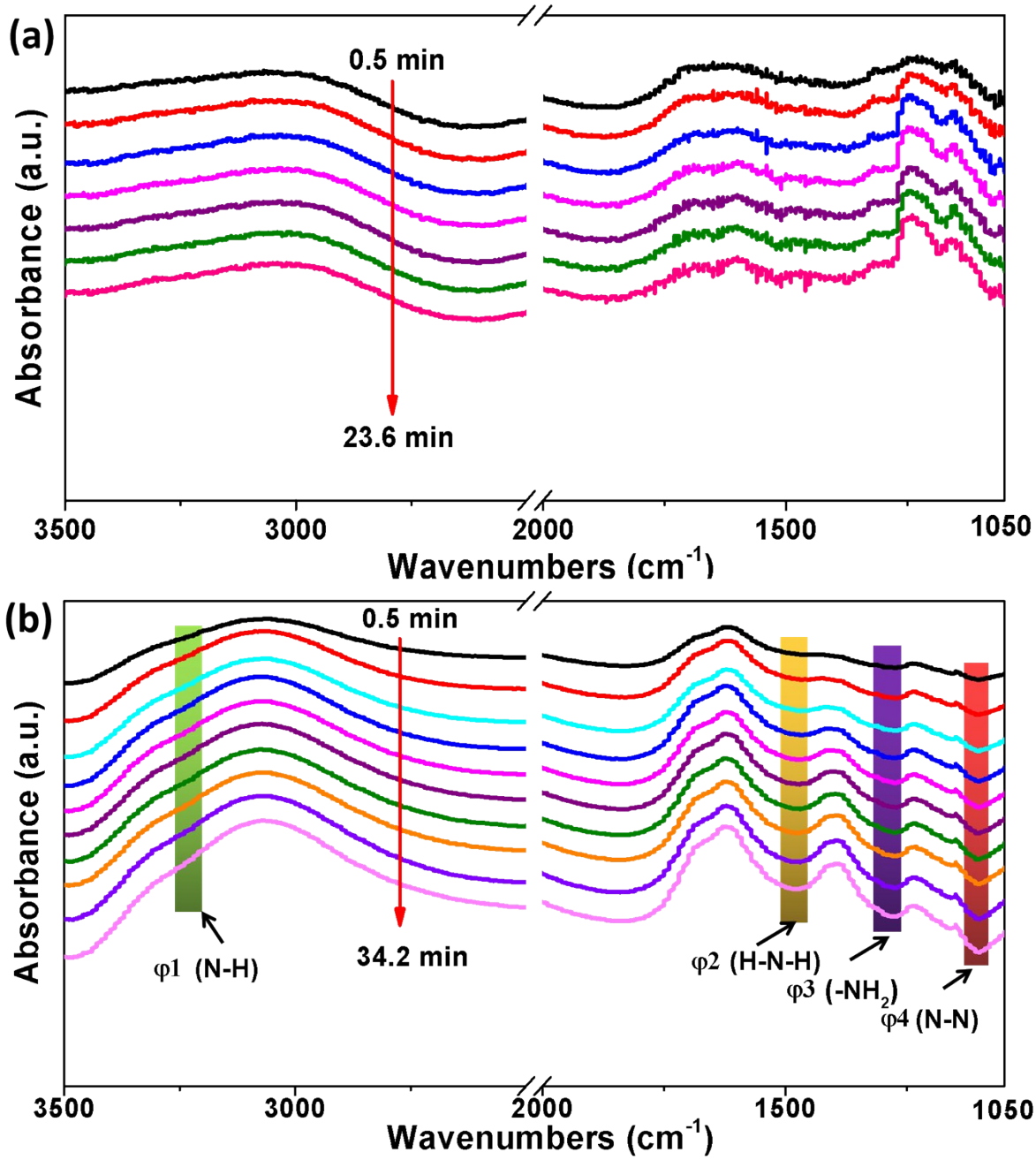

Fig. S37 Electrochemical *in situ* FTIR spectra of the NRR on the S3/ZIF-8 in (a) Ar-bubbled 0.1 M KOH and (b) N_2-bubbled 0.1 M KOH.

Table S1. Summary of the NRR performances for some reported state-of-the-art electrocatalysts in N_2-saturated electrolytes.

Catalyst	Electrolyte	NH_3 yield	FE (%)	Ref.
S3/ZIF-8	0.1 M HCl	63.9 μg h^{-1} $mg^{-1}_{cat.}$ = 1.3 × 10^{-9} mol s^{-1} cm^{-2}	14.2	This work.
S3/ZIF-8	0.1 M Na_2SO_4	14.5 μg h^{-1} $mg^{-1}_{cat.}$	6.7	This work.
S3/ZIF-8	0.1 M KOH	12.1 μg h^{-1} $mg^{-1}_{cat.}$	4.2	This work.
Au/Ti_3C_2	0.1 M HCl	30.06 μg h^{-1} $mg^{-1}_{cat.}$	18.34	[8]
Au flowers	0.1 M HCl	25.57 μg h^{-1} $mg^{-1}_{cat.}$	6.05	[9]
Au/TiO_2	0.1 M HCl	21.40 μg h^{-1} $mg^{-1}_{cat.}$	8.11	[10]
a-Au/CeO_x–RGO	0.1 M HCl	8.3 μg h^{-1} $mg^{-1}_{cat.}$	10.10	[11]
PdRu BPNs	0.1 M HCl	25.92 μg h^{-1} $mg^{-1}_{cat.}$	1.53	[12]
PdRu NRAs	0.1 M HCl	34.2 μg h^{-1} $mg^{-1}_{cat.}$	2.4	[13]
Cr_2O_3-rGO	0.1 M HCl	33.3 μg h^{-1} $mg^{-1}_{cat.}$	7.33	[14]
Nb_2O_5 nanofiber	0.1 M HCl	43.6 μg h^{-1} $mg^{-1}_{cat.}$	9.26	[15]
MoO_3 nanosheets	0.1 M HCl	29.43 μg h^{-1} $mg^{-1}_{cat.}$	1.9	[16]
Fe_3S_4 nanosheets	0.1 M HCl	75.4 μg h^{-1} $mg^{-1}_{cat.}$	6.45	[17]
Mo_2C nanorod	0.1 M HCl	95.1 μg h^{-1} $mg^{-1}_{cat.}$	8.13	[18]
NPC	0.1 M HCl	0.97 μg h^{-1} $mg^{-1}_{cat.}$	4.2	[19]
O-CN	0.1 M HCl	20.15 μg h^{-1} $mg^{-1}_{cat.}$	4.97	[20]
S-G	0.1 M HCl	27.3 μg h^{-1} $mg^{-1}_{cat.}$	11.5	[21]
h-BNNS	0.1 M HCl	22.4 μg h^{-1} $mg^{-1}_{cat.}$	4.7	[22]
B_4C	0.1 M HCl	26.57 μg h^{-1} $mg^{-1}_{cat.}$	15.95	[23]

B_4C-BGQDs	0.1 M HCl	28.6 μg h^{-1} $mg^{-1}_{cat.}$	16.7	[24]
PCN	0.1 M HCl	8.09 μg h^{-1} $mg^{-1}_{cat.}$	11.59	[25]
Bi NS/CF	0.1 M HCl	6.89×10^{-11} mol s^{-1} cm^{-2}	10.26	[26]
Ag nanosheet	0.1 M HCl	4.62×10^{-11} mol s^{-1} cm^{-2}	4.8	[27]
d-TiO_2/TM	0.1 M HCl	1.24×10^{-10} mol s^{-1} cm^{-2}	9.17	[28]
MoN NA/CC	0.1 M HCl	1.47×10^{-10} mol s^{-1} cm^{-2}	1.15	[29]
VN/CC	0.1 M HCl	2.48×10^{-10} mol s^{-1} cm^{-2}	3.58	[30]

Table S2. Summary of the NRR performances for some reported state-of-the-art electrocatalysts in air-saturated electrolytes.

Catalyst	Electrolyte	NH_3 yield	Ref.
S3@ZIF-8	0.1 M HCl	23.3 μg h^{-1} $mg^{-1}_{cat.}$ = 1.3× 10^{-9} mol s^{-1} cm^{-2}	This work.
S-CNS/CP	0.1 M Na_2SO_4	10.82 μg h^{-1} $mg^{-1}_{cat.}$	[31]
$Fe_2O_3/TiO_2/C$	1.0 M KOH	5.72 × 10^{-11} mol mg^{-1} s^{-1}	[32]
Pt/C	0.001 M H_2SO_4	1.14 × 10^{-9} mol s^{-1} cm^{-2}	[33]

Table S3. Energetic data pertaining to key steps of N_2 reduction by H_2 on CuAu (111).

Elemental step	ΔE (eV)	ΔZPE (eV)	$T\Delta S$ (eV)	ΔG (eV)
$N_2+*\rightarrow N_2^*$	-0.18	0.01	-0.27	0.09
$N_2^*+H^*\rightarrow NNH^*+*$	1.72	0.15	-0.14	2.01
$NNH^*+H^*\rightarrow NHNH^*+*$	-0.70	0.15	0.01	-0.56
$NHNH^*+H^*\rightarrow NH_2NH^*+*$	-0.80	0.19	0.07	-0.68
$NH_2NH^*+H^*\rightarrow NH_2NH_2^*+*$	-1.36	0.16	0.09	-1.29
$NH_2NH_2^*+H^*\rightarrow NH_3NH_2^*+*$	-0.21	0.11	-0.01	-0.10
$NH_3NH_2^*+H\rightarrow 2NH_3^*+*$	-2.08	0.04	0.05	-2.09
$2NH_3^*\rightarrow 2NH_3+2*$	0.49	-0.07	0.84	-0.42
$N_2^*\rightarrow 2N^*$	5.04	0.19	-0.24	5.47
$NNH^*+H^*\rightarrow NNH_2^*+*$	-0.41	0.13	0.09	-0.37

References

[1] G. Kresse and J. Hafner, *Phys. Rev. B* 1994, **49**, 14251.

[2] G. Kresse and J. Furthmüller, *Comp. Mater. Sci.* 1996, **6**, 15-50.

[3] J. P. Perdew, K. Burke and M. Ernzerhof, *Phys. Rev. Lett.* 1996, **77**, 3865.

[4] P. E. Blöchl, *Phys. Rev. B* 1994, **50**, 17953.

[5] G. Kresse, D. Joubert, *Phys. Rev. B* 1999, **59**, 1758.

[6] H. J. Monkhorst, J. D. Pack, *Phys. Rev. B* 1976, **13**, 5188.

[7] A. A. Gokhale, S. Kandoi, J. P. Greeley, M. Mavrikakis and J. A. Dumesic, *Chem. Eng. Sci.* 2004, **59**, 4679-4691.

[8] D. Liu, G. Zhang, Q. Ji, Y. Zhang and J. Li, *ACS Appl. Mater. Inter.* 2019, **11**, 25758-25765.

[9] Z. Wang, Y. Li, H. Yu, Y. Xu, H. Xue, X. Li, H. Wang and L. Wang, *ChemSusChem* 2018, **11**, 3480-3485.

[10] M. M. Shi, D. Bao, B. R. Wulan, Y. H. Li, Y. F. Zhang, J. M. Yan and Q. Jiang, *Adv. Mater.* 2017, **29**, 1606550.

[11] S. J. Li, D. Bao, M. M. Shi, B. R. Wulan, J. M. Yan and Q. Jiang, *Adv. Mater.* 2017, **29**, 1700001.

[12] Z. Wang, C. Li, K. Deng, Y. Xu, H. Xue, X. Li, L. Wang and H. Wang, *ACS Sustain. Chem. Eng.* 2018, **7**, 2400-2405.

[13] H. Wang, Y. Li, D. Yang, X. Qian, Z. Wang, Y. Xu, X. Li, H. Xue and L. Wang, *Nanoscale* 2019, **11**, 5499-5505.

[14] L. Xia, B. Li, Y. Zhang, R. Zhang, L. Ji, H. Chen, G. Cui, H. Zheng, X. Sun and F. Xie, *Inorg. Chem.* 2019, **58**, 2257-2260.

[15] J. Han, Z. Liu, Y. Ma, G. Cui, F. Xie, F. Wang, Y. Wu, S. Gao, Y. Xu and X. Sun, *Nano Energy* 2018, **52**, 264-270.

[16] J. Han, X. Ji, X. Ren, G. Cui, L. Li, F. Xie, H. Wang, B. Li and X. Sun, *J. Mater. Chem. A* 2018, **6**, 12974-12977.

[17] X. Zhao, X. Lan, D. Yu, H. Fu, Z. Liu and T. Mu, *Chem. Commun.* 2018, **54**, 13010-13013.

[18] H. Cheng, L. X. Ding, G. F. Chen, L. Zhang, J. Xue and H. Wang, *Adv. Mater.* 2018, **30**, 1803694.

[19] P. Song, H. Wang, L. Kang, B. Ran, H. Song and R. Wang, *Chem. Commun.* 2019, **55**, 687-690.

[20] H. Huang, L. Xia, R. Cao, Z. Niu, H. Chen, Q. Liu, T. Li, X. Shi, A. M. Asiri and X. Sun, *Chem. Eur. J.* 2019, **25**, 1914-1917.

[21] L. Xia, J. Yang, H. Wang, R. Zhao, H. Chen, W. Fang, A. M. Asiri, F. Xie, G. Cui and X. Sun, *Chem. Commun.* 2019, **55**, 3371-3374.

[22] Y. Zhang, H. Du, Y. Ma, L. Ji, H. Guo, Z. Tian, H. Chen, H. Huang, G. Cui and A. M. Asiri, *Nano Res.* 2019, **12**, 919-924.

[23] W. Qiu, X.-Y. Xie, J. Qiu, W.-H. Fang, R. Liang, X. Ren, X. Ji, G. Cui, A. M. Asiri and G. Cui, *Nat. Commun.* 2018, **9**, 3485.

[24] W. Qiu, Y.-X. Luo, R.-P. Liang, J. Qiu and X.-H. Xia, *Chem. Commun.* 2019, **55**, 7406-7409.

[25] C. Lv, Y. Qian, C. Yan, Y. Ding, Y. Liu, G. Chen and G. Yu, *Angew. Chem. Int. Ed.* 2018, 57, 10246-10250.

[26] R. Zhang, L. Ji, W. Kong, H. Wang, R. Zhao, H. Chen, T. Li, B. Li, Y. Luo and X. Sun, *Chem. Commun.* 2019, **55**, 5263-5266.

[27] H. Huang, L. Xia, X. Shi, A. M. Asiri and X. Sun, *Chem. Commun.* 2018, **54**, 11427-11430.

[28] L. Yang, T. Wu, R. Zhang, H. Zhou, L. Xia, X. Shi, H. Zheng, Y. Zhang and X. Sun, *Nanoscale* 2019, **11**, 1555-1562.

[29] L. Zhang, X. Ji, X. Ren, Y. Luo, X. Shi, A. M. Asiri, B. Zheng and X. Sun, *ACS Sustain. Chem. Eng.* 2018, **6**, 9550-9554.

[30] X. Zhang, R.-M. Kong, H. Du, L. Xia and F. Qu, *Chem. Commun.* 2018, **54**, 5323-5325.

[31] L. Xia, X. Wu, Y. Wang, Z. Niu, Q. Liu, T. Li, X. Shi, A. M. Asiri and X. Sun, *Small Methods* 2018, 1800251.

[32] R. Manjunatha, A. Karajić, V. Goldstein and A. Schechter, *ACS Appl. Mater. Inter.* 2019, **11**, 7981-7989.

[33] R. Lan, J. T. Irvine and S. Tao, *Scientific Rep.* 2013, **3**, 1145.